SUPPLEMENTARY MATERIALS FOR:

The role of mixing and crystallization in the differentiation of magmatic systems

Lea Ostorero[1,2*], Daniele Morgavi[3], Fabio Arzilli[4], Georges Boudon[1], Maurizio Petrelli[5], Alessandro Pisello[5], Diego Perugini[5], Luigi Franciosi[3], Hélène Balcone-Boissard[6]

[1]Université Paris Cité, Institut de physique du globe de Paris, CNRS, F-75005 Paris, France

[2]Now at Department of Earth and Environmental Sciences, University of Milano-Bicocca, Milan, Italy

[3]Dipartimento di Scienze della Terra, dell'Ambiente e delle Risorse, Università degli Studi di Napoli Federico II, Via Vicinale Cupa Cintia 21, Naples 80126, Italy

[4]School of Science and Technology, Geology Division, University of Camerino, Camerino, Italy

[5]Department of Physics and Geology, University of Perugia, Piazza Universitá, Perugia 06100, Italy

[6]Institut des Sciences de la Terre de Paris (ISTeP), UMR 7193, CNRS-Sorbonne Université, Paris, France

Supplementary Note

Material and methods

Preparation of the synthetic basalt

The synthetic basalt composition is equivalent in composition to a basaltic enclave in a lava flow of Kizimen of Quaternary age (Kiz-01/1)[1,2] (**Supplementary Table 1**). This basaltic end-member has been obtained by mixing oxides powders in the laboratory at the Department of Physics and Geology (University of Perugia, Italy) (Na_2O and in K_2O were converted in sodium and potassium carbonates (Na_2CO_3 and K_2CO_3); all FeO was converted in Fe_2O_3 and no MnO and P_2O_5 were added). After grinding with an agate mortar, a fine powder was obtained.

Theoretical viscosities of the end-members

Based on the starting materials compositions (**Supplementary Table 1**), we calculated the theoretical viscosity evolution of each end-member between 1100-1250 °C[3]. We also show the evolution of the viscosity for the bulk synthetic basalt and dacite and the melts using the data calculated with Rhyolite-MELTS v.1.2 software[4], with the effect of the presence of crystals (**Supplementary Fig. 7**).
For the experiment here, the degree of undercooling is of 27 ± 0.5 °C (liquidus temperature of the feldspar from Rhyolite-MELTS calculations of 1227 °C and final temperature of the system of 1200 ± 0.5 °C)[4].

High-temperature magma mixing experiment

The Chaotic Magma Mixing Apparatus (hereafter COMMA) experimental device is presented in details in another study[5] and the method described further down is from the same study. Two parameters define the COMMA geometry: (1) the ratio of the radii between the two cylinders ($r = \frac{R_{sp}}{R_{out}} = \frac{1}{3}$) and (2) the eccentricity ratio to the outer cylinder ($\varepsilon = \frac{\delta}{R_{out}} = 0.3$), where δ is the distance between the centers of the inner and outer cylinders (**Fig. 2c**)[5].
Three main objectives are accomplished by the device: (a) allow independent rotations of the inner and outer cylinders, at variable speeds, directions and stirring protocols allowing to trigger chaotic mixing[6], (b) to put the apparatus in the hot spot region of a well-calibrated high-temperature furnace (up to 1800 °C) and (c) finally to cool rapidly the silicate melts after the application of the mixing protocol to freeze in time the evolution of the mixing process, avoiding any crystallization of the sample. Two cylinders were drilled out of the crucible with the dacitic melt to have the required geometric configuration for the experiment: one cylinder for the spindle and a second cylinder for the initial position of the second end-member (synthetic basalt). The crucible (outer cylinder) is then connected to the motor above the furnace and was located off-center. Two alumina (Al_2O_3) rods are fixed to the upper and lower motor axis to act as the inner cylinder and holding the crucible (respectively). The lower end of the upper alumina rod is sheathed with a spindle ($Pt_{80}Rh_{20}$) to prevent from any contamination of the silicate melts during the experimental runs. Pt-PtRh thermocouples (accuracy ± 0.5 °C) are used to measure the temperature within the samples during the experiment (via the alumina rod). The vertical movement of the furnace allows to prepare the setup of the experiment by positioning the outer and inner cylinders outside the furnace. The furnace is then brought to the experimental temperature when the sample is still outside of the furnace (1200 °C). The furnace is then moved quickly in the end position required to do the experiment to minimize the time of attainment of thermal equilibrium (~10-15 min) in the

sample. When the thermocouples inside the spindle measure the experimental temperature, the experiment is initiated by turning on the experimental mixing protocol.

The computer-controlled mixing protocol consists of a combination of separated alternating rotations of outer and inner cylinders in this sequence:

(i) 2 complete rotations of the outer cylinder in 7 h and 10 min
(ii) 6 complete rotations of the inner cylinder in 3h and 20 min.

The mixing experiment lasted ten and half hours. The main experimental parameters characterizing the COMMA experiment are summarized in **Supplementary Table 6**.
For the experiment, we can calculate the shear rate with the following equation:

$$\gamma = \frac{\pi * D * N}{60h} \quad (1)$$

with the diameter D in mm, N velocity angle in rpm and h the depth of the cylinder in mm[7,8].
At the end of the experiment, the furnace holding the experimental crucible was quickly moved vertically while maintaining the crucible and the spindle in their original positions[5,9]. This final step allows a rapid quenching of the experimental melt (cooling rate of 41 °C/min) to form a glassy experimental product[9]. After the experiment, quenched glasses are cored out from the outer cylinder and set in epoxy. They are then cut into slices of 2-4 mm thickness and analyzed by Scanning Electron Microscope (SEM) and Electron Probe Micro-analyzer to study the patterns generated by the mixing process and the space and time variability of chemical exchanges between the melts.

Crystal Size Distribution

SEM images were analyzed with *ImageJ* software (https://imagej.nih.gov/ij/; version 1.52a), applying a threshold on the greyscale to select the microlites and then displaying the analyzed particles as a mask. Images were then processed with *JMicrovision* (https://jmicrovision.github.io/; version 1.3.4) to measure the length, width, area of microlites and orientation (vesicle-free), with the edge-intersecting crystals that were removed. To convert two-dimensional textural data to three-dimensional data, the average crystal aspect ratio of each sample was obtained using a spreadsheet, *CSDSlice* (version 5)[10]. This aims to compare the 2D measurements with 2D ideal shape curves from a database of thousands of random sections through known shapes, to identify five best-fitting curves and the corresponding crystal aspect ratios based on a least-square fit between the sample and the database[10,11]. More than 400 crystals were measured[10]. R^2 of the best-fit was over 0.8, meaning a reliable statistical fit (**Supplementary Table 3**).
The crystal fraction was calculated on a vesicle-free basis:

$$\varphi = \frac{A_{crystal}}{A_T} \quad (2)$$

Where $A_{crystal}$ is the area of the crystal phase and A_T is the total area of the images studied. The two-dimensional crystal number density N_a (mm^{-2}) was obtained by dividing the number of microlites by the total area analyzed, free of vesicles[12].
The software *CSDCorrections* (http://www.uqac.ca/mhiggins/csdcorrections.html; version 1.55) was then used to obtain information on crystal population density and crystal sizes[13,14] (**Supplementary Table 4**). The number density of crystals *n* is a linear function of crystal size *L*, expressed as follows:

$$n = n^0 e^{\frac{-L}{G\,\tau}} \quad (3)$$

Where n^0 is the nucleation density of the curve of the crystal size distribution, for L = 0, G the growth rate and τ the residence time[13]. This curve, when plotted in logarithmic, gives us access to the timescales of magmatic processes by using the linear relation between the crystal population density and the crystal length, as the slope of the correlation is equal to[13,15]:

$$slope = -\frac{1}{G * \tau} \quad (4)$$

The three-dimensional crystal number density N_v (mm^{-3}) was obtained with *CSDCorrections*[13,14], which adds the number of crystals in each bin interval after the stereological correction with *CSDSlice*[10]. The characteristic length of the microlites L_C, is also estimated by *CSDCorrections* ($L_C = -\frac{1}{slope}$).

Geochemical compositions of the glasses, transects and crystals

Whole rock and glass compositions

In the Total alkali diagram, the starting materials compositions are in the basaltic and dacitic field, respectively (51.3 wt% SiO_2 and 4 wt% Na_2O+K_2O and 64 wt% SiO_2 and 5.4 wt% Na_2O+K_2O) (**Fig. 5**). The main glasses of all zones in the experimental sample are between 55-66 wt% in SiO_2 and 3.5-6 wt% in $Na_2O+ K_2O$ (**Fig. 5**).

Transects

The compositional variability was studied along several compositional transects (**Supplementary Table 2**). These transects were done to cover different areas of the mixing patterns developed in the experiment: crossing different mafic filaments with isolated crystals in them or without crystals and also in felsic parts in the crystallized enclaves (**Fig. 9**). **Fig. 9** shows oscillatory patterns as passing through filaments of the two different melts, with lower compositions in SiO_2 than the dacite but higher than the synthetic basalt. The mafic compositions are not the same depending on the three transects (for example, on **Fig. 9a, e, i**, SiO_2 content is mainly varying from 60, 57, 59 wt%, respectively and 3.6, 5 and 4 wt% in MgO) whereas the felsic components are between 64-65 wt% for SiO_2 respectively and around 2.5 wt% in MgO. **Fig. 9** shows the compositions of the transects, with the SiO_2 content mainly varying from 62-65 wt%, CaO content between 5-6 wt%, MgO between 2-3 wt% and FeO between 5-6 wt%. Some variations occur, with lower values reached for the SiO_2, MgO and FeO_{tot} content and higher values for the CaO content (**Fig. 9a-l**). Mafic compositions have a very low representativity as seen on **Supplementary Fig. 3**, with only a few points between 51-53 wt% in SiO_2 and between 5-6 wt% in MgO.
Harker diagrams show the compositional variability of these glasses, with the compositions mainly covering the areas between 55-65 wt% in SiO_2, 5-8 wt% in CaO, 2-6 wt% in MgO, 1-2.5 wt% in K_2O, 2.5-4 wt% in Na_2O and 16-18 wt% in Al_2O_3 (**Fig. 6**). Practically no mafic glass is present in the range of the compositions from the synthetic basalt to the most mafic glass generated by the experiment, with only a few points being in this interval (from 51-55 wt% in SiO_2, for example).

Near crystallized areas

The glasses in the crystallized enclaves also show variations, with the cores of these zones being more mafic than the margins (mainly between 53-60 wt% compared to 56-64 wt% in SiO_2) (**Supplementary Fig. 3**). The felsic parts in the crystallized enclaves also sampled some more mafic areas (56 wt% in SiO_2) (**Fig. 6a-f**). The basaltic remains are nearly absent whereas dacitic areas are dominant, as well as hybrid zones (**Fig. 6a-f**).
Comparing the experimental glasses with the natural ones, the residual glasses from the natural banded andesites of Kizimen are rhyolitic whereas the experimental ones are from basaltic andesites to dacites (**Fig. 5**).

CSD results

The plagioclase crystal fraction was estimated at 23 vol%, with an approximated tabular dominant shape and a mean orientation of -58° (**Fig. 8; Supplementary Fig. 6; Supplementary Table 3-4**). In two dimensions, these crystals show an abundant growth but limited nucleation during the experiment (crystal number density N_a of ~140 mm^{-2}; **Supplementary Fig. 6; Supplementary Note**). The CSD curve shows a size distribution of the crystals from 0.02 mm to 1.2 mm, with a characteristic length of 0.15 mm (**Fig. 8a; Supplementary Table 3**). The CSD curve of the experimental sample can be approximated as a straight line (**Fig. 8a**), it implies that nucleation and growth were continuous during crystallization during the experiment. Compared to **Supplementary Fig. 6**, where it indicated abundant growth and limited nucleation, the two types of information are not coherent; this shows the importance of confronting several types of data. CSD results, where 2D data were converted in 3D is more trustworthy (**Supplementary Table 3-4**)[13,14], so we conclude that nucleation and growth were continuous during crystallization.

Supplementary Figures

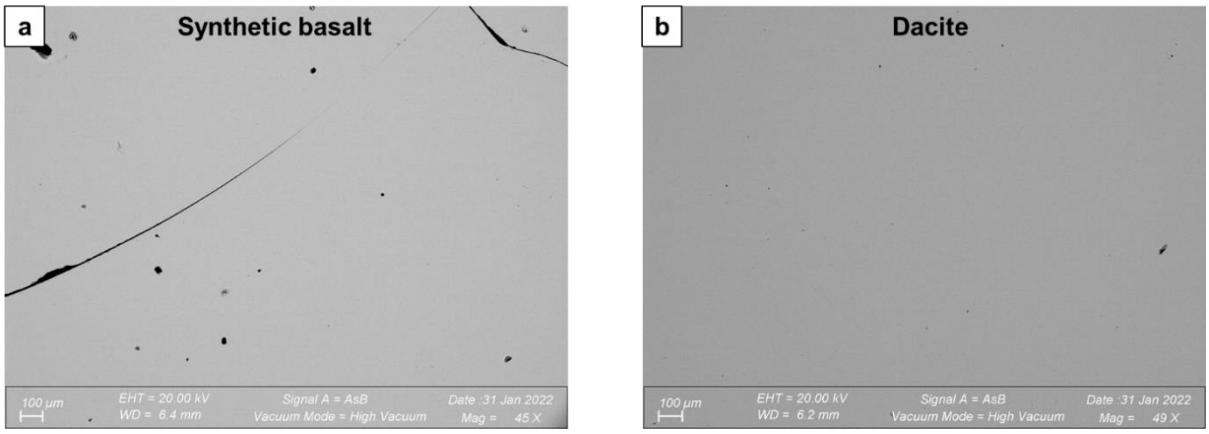

Supplementary Fig. 1: Back-scattered electron (BSE) images of the homogenized starting materials of the experiment after the melting process in the furnace. a) Synthetic basalt and b) Dacite.

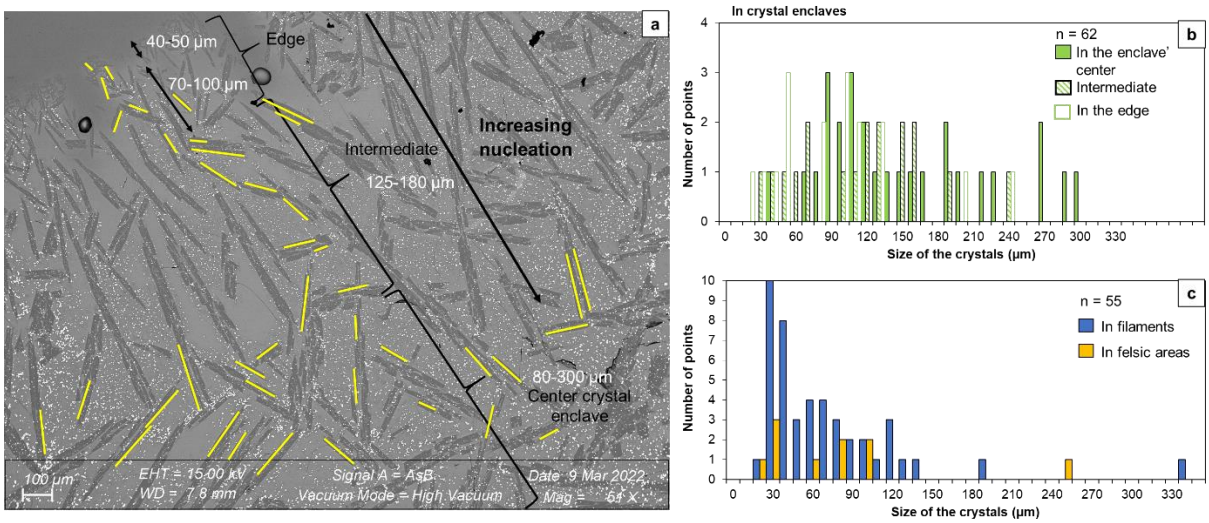

Supplementary Fig. 2: Evolution of the sizes of the crystals depending on their location in the experimental sample. a) BSE image of a crystal enclave with the margins (with small crystals), intermediate zone and center, with increasing size of the crystals (measured with *ImageJ*; https:// imagej. nih. gov/ ij/; version 1.52a). b) Size of the crystals in the crystal enclaves, in the center of the enclaves, intermediate part or the edges. c) Size of the crystals in the filaments or in the felsic areas. The preferred orientation of the crystals is shown in yellow in (a). n is the number of crystals where the size was measured.

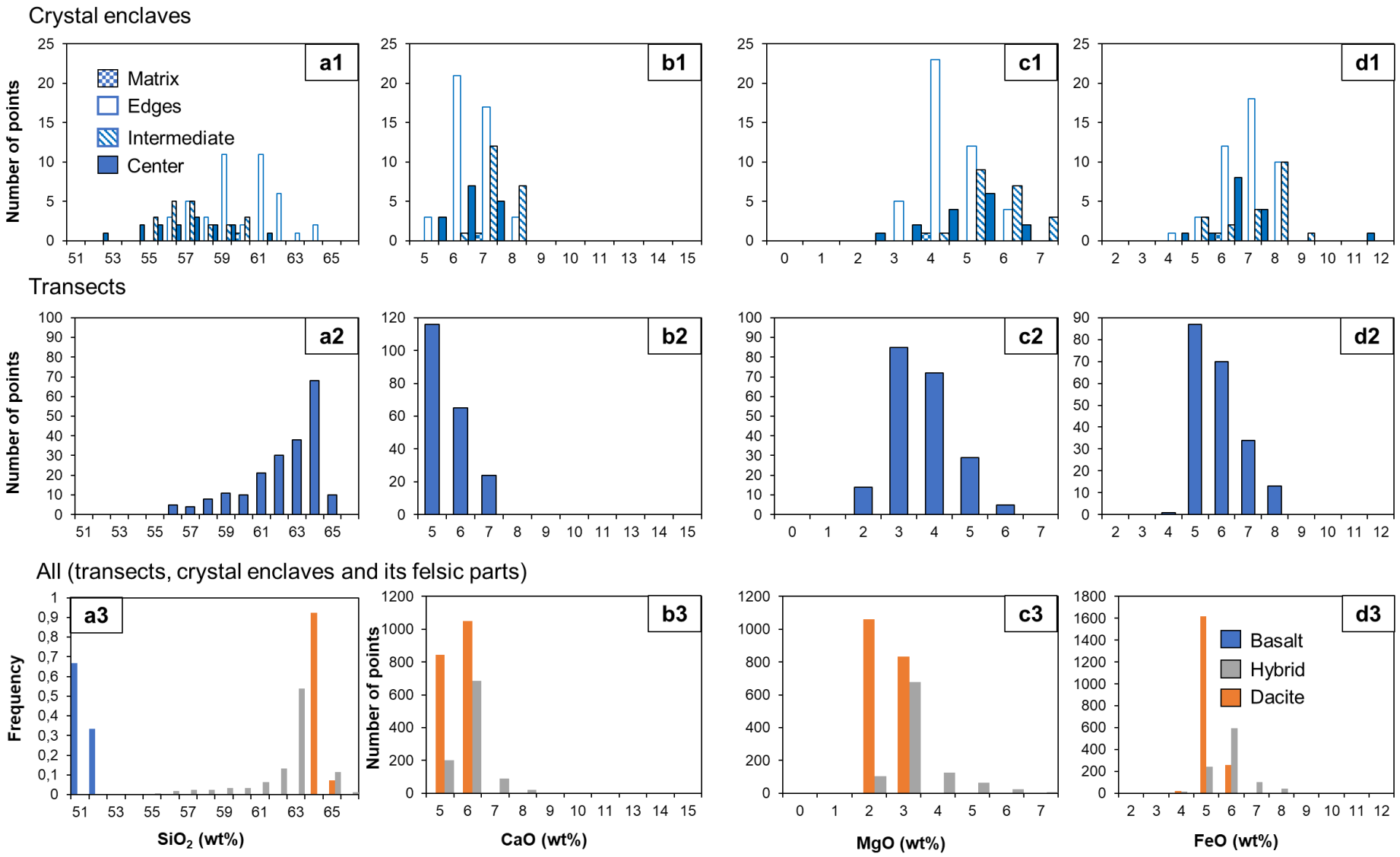

Supplementary Fig. 3: a1-d1) Compositions of the residual glasses of the crystal enclaves of the experiment for major elements. a) SiO_2, b) CaO, c)

MgO, d) FeO, depending on the location of the measure (on the exterior, edges, intermediate or center of the crystal enclave, see **Supplementary Fig. 2** for the definition of these areas) and a2-d2) for felsic areas in crystallized enclaves. a3-d3) All the compositions (of the transects, crystals enclaves and felsic parts in the crystallized enclaves) are classified in three types: basalt, hybrid and dacite, depending on their relative compositions.

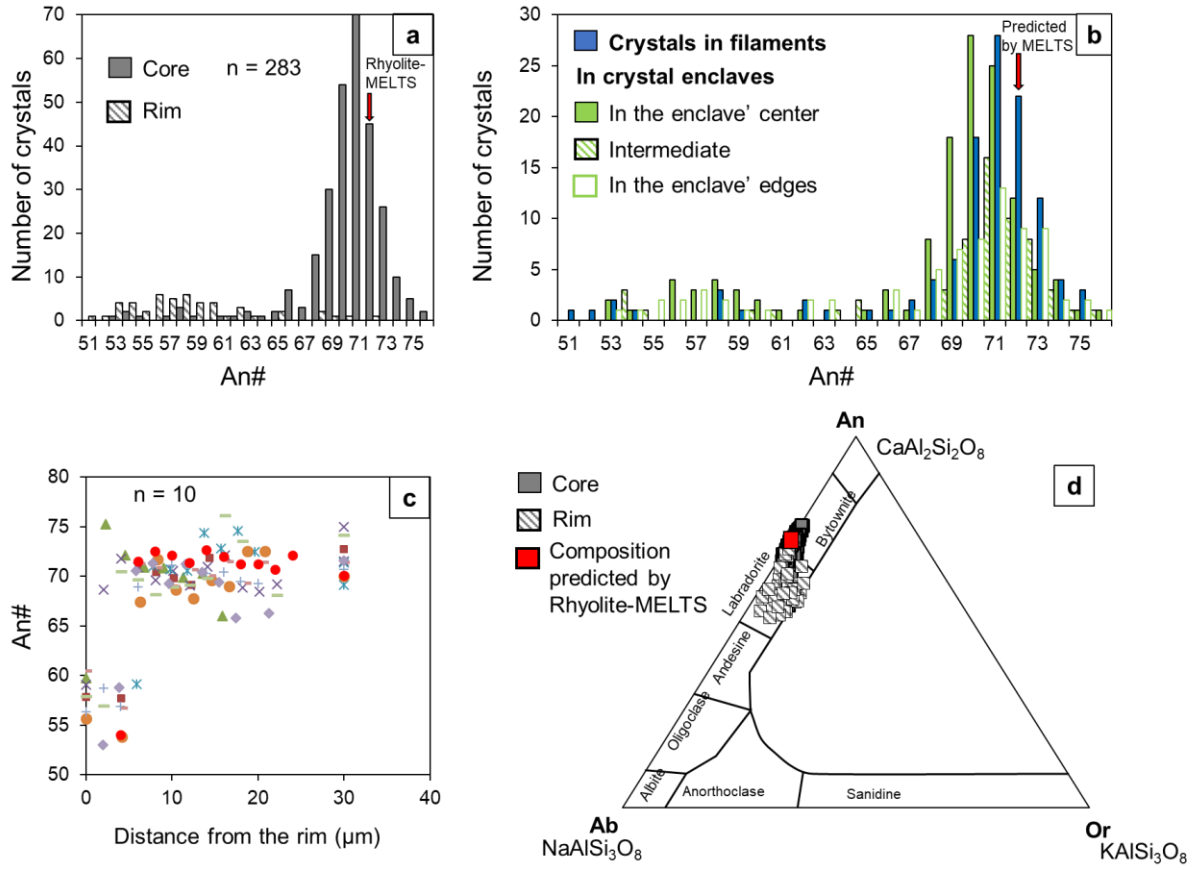

Supplementary Fig. 4: Compositions of the experimental plagioclase crystals. a) Compositional histogram of the An# content of the cores and rims of the plagioclase crystals. b) Histogram of the An# of the plagioclase crystals depending on their locations (in crystal enclaves or filaments). c) Examples of transects done in the plagioclase crystals. d) Ternary diagram of the plagioclase crystals[16]. The An# predicted by Rhyolite-MELTS software for the synthetic basalt at 1200 °C and NNO+2 is also shown[4]. n is the number of crystals analyzed.

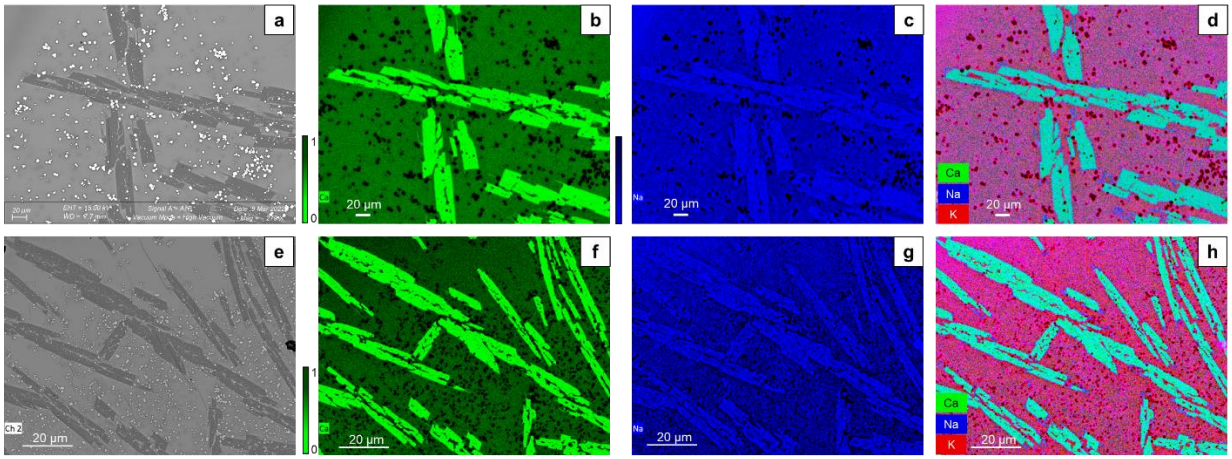

Supplementary Fig. 5: Chemical maps of the experimental plagioclase crystals. a and e) in grey intensities, b and f) Ca mapping, c and g) Na mapping and d and h) Ca, Na and K maps in Red-Green-Blue (RGB).

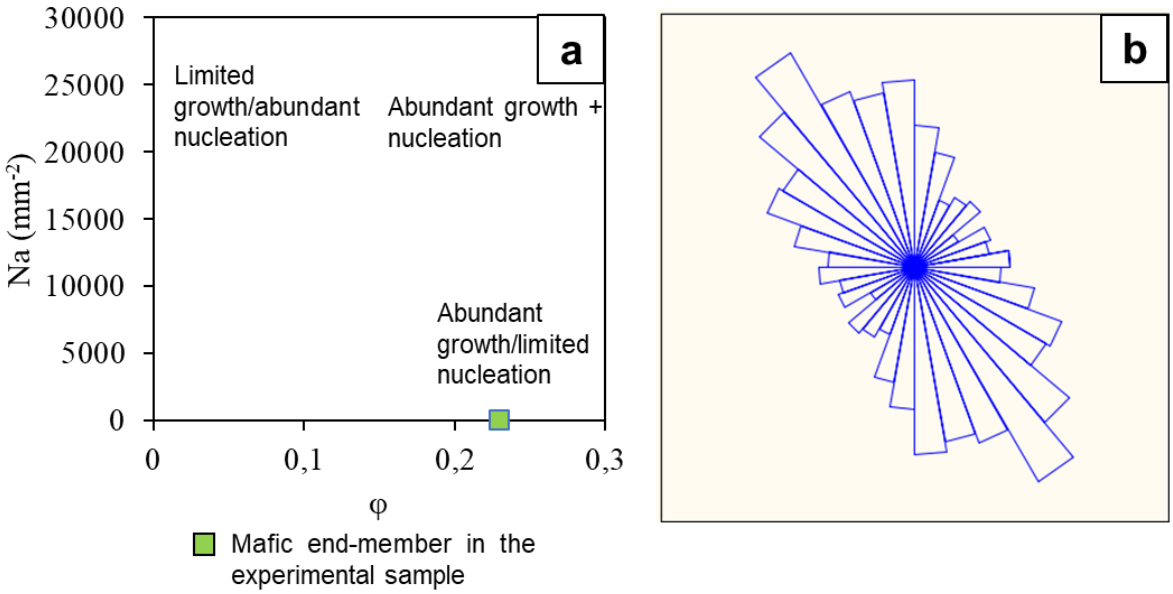

Supplementary Fig. 6: 2D Microlite number density versus the crystal fraction crystal microlite content φ (a) and (b) orientations of the plagioclase crystals in the mafic part in the experiment. On (a), the graph allows to show different dynamics in nucleation and growth in the systems that are specified on the plot. Data in the lower right-hand corner correspond to abundant growth but limited nucleation, whereas data in the upper right-hand corner are linked to processes where nucleation and growth were abundant, and finally, in the upper left hand-corner of the graph, nucleation is abundant but not growth[11] (**Supplementary Table 3**). b) Rose diagram of crystals orientation. The mean orientation is measured with respect to the X-axis in a counter-clockwise direction[13].

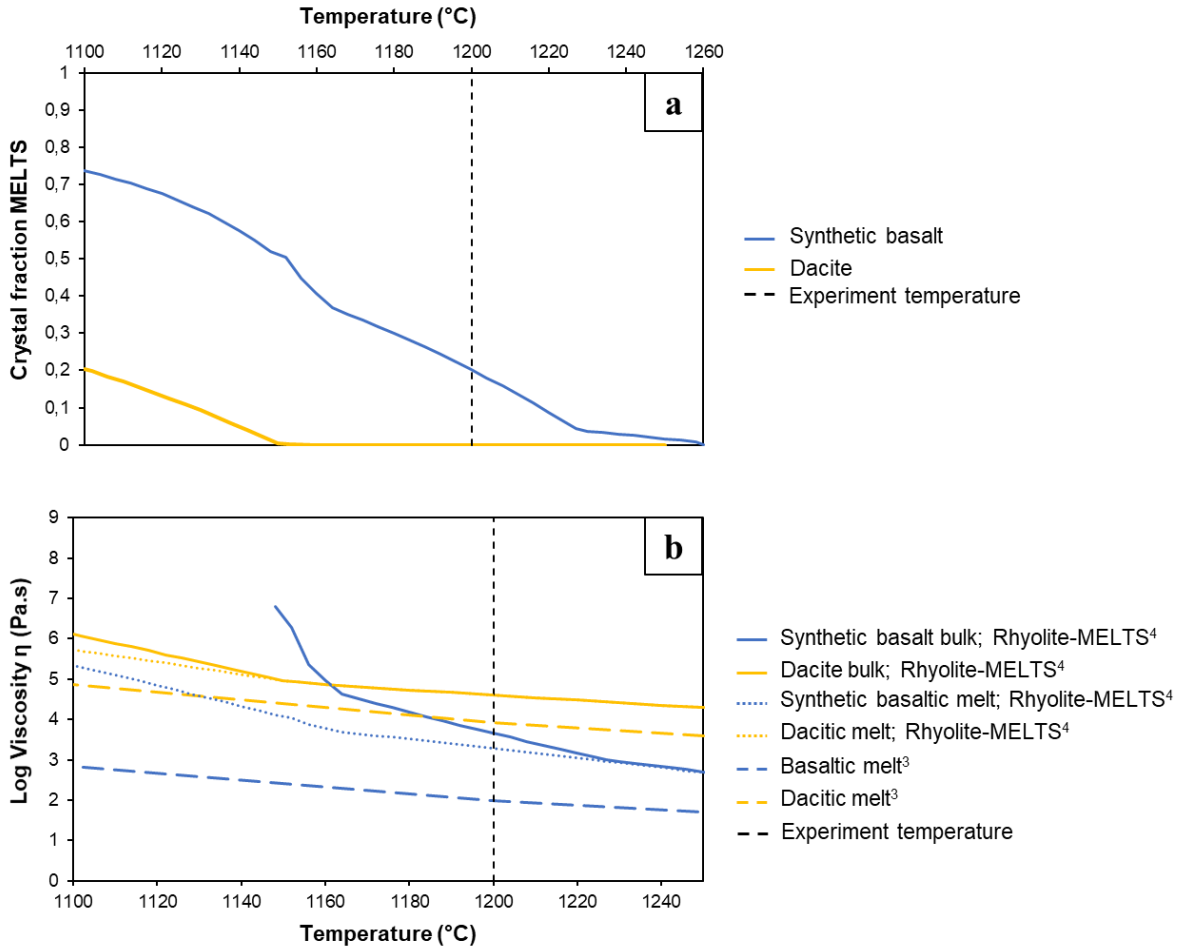

Supplementary Fig. 7: Crystal fractions and viscosities. a) Theoretical crystal fraction of the synthetic basalt and dacite depending on the temperature (°C), given by Rhyolite-MELTS software at NNO+2 conditions[4]. b) Melt and bulk viscosities given by Rhyolite-MELTS software[4] considering the crystal fraction. The bulk viscosities of the two end-members cross at a temperature close to 1170 °C. The viscosities of the two end-members calculated using a viscosity model are also shown[3]. The temperature used during the experiment (1200 °C) is highlighted with a dotted line.

Supplementary Tables

Oxide	KIZ-96-01/1 (wt%) [1]	Synthetic basalt	Error min	Error max	Dacite	Error min	Error max
SiO_2	49.7	51.28	0.66	0.85	64.16	0.67	0.69
TiO_2	1.22	1.25	0.34	0.28	0.61	0.19	0.13
Al_2O_3	18.84	19.25	0.64	0.71	16.58	0.57	0.41
Fe_2O_3	5.32						
FeO	5.56	10.55	0.63	0.54	5.26	0.59	0.35
MnO	0.19	0.02	0.08	0.08	0.11	0.15	0.14
MgO	5.2	5.32	0.31	0.31	2.38	0.12	0.16
CaO	9.25	8.43	0.39	0.53	5.34	0.2	0.28
Na_2O	2.74	3.08	0.24	0.41	3.64	0.54	0.25
K_2O	0.76	0.76	0.13	0.18	1.76	0.21	0.28
P_2O_5	0.17	0.04	0.08	0.14	0.17	0.19	0.15
LOI	0.73						
Total	99.67	100			100		

Supplementary Table 1: Major elements composition of the basaltic enclave of Kizimen (KIZ-96-01/1)[1] that was reproduced through the synthetic basalt and the starting material compositions of the synthetic basalt and dacite, with the positive and negative errors.

Supplementary Table 2: Excel file with major element analyses (wt%) in the glasses of the experimental samples (in crystal enclaves, filaments) or in crystals (cores, rims or edges). Names of the samples: slices 2 or 3 of the experimental samples. The 38 transects performed through the filaments are also shown.

Sample	Number of crystals	ϕ	Na (mm^{-2})	Best-fit crystal habit (x, y, z)	score (R^2)	S/M	S/L	M/L
Experiment	458	0,23	138	1 : 4 : 9	0,88	0,25	0,11	0,44

Supplementary Table 3: Number of crystals, microlite crystal fraction φ, two-dimensional crystal number density N_a, best-fit crystal habit using *CSDSlice*[10] for the experimental and natural samples and the associated R^2 and the aspect ratios (short axis over medium axis (S/M), short axis over long axis (S/L) and medium axis over long axis (M/L)).

Sample	Mean Orientation (°)	Ratio orientation ellipse axes	Alignment factor	Nv (mm^{-3})	Lc (mm) (1σ error)	Intercept (1σ error)	Slope (1σ error)
Experiment	-58	0,75	0,28	$1{,}10.10^3$	0,1505 (0,02)	9,25 (0,08)	- 7.69 (0.25)

Supplementary Table 4: Data obtained from *CSDCorrections*[13,14], the mean orientation, alignment factor, three-dimensional crystal number density N_v, characteristic length L_c, intercepts and slopes of the CSD (with the associated 1σ error).

	Experimental growth rate *G* (cm/s)	Timescale of crystal growth from eq. 1 (h)
G^{66}	$7.74.10^{-5}$	0,05 (3 min)
G^{50}	2.10^{-6}	1,81

Supplementary Table 5: Estimation of timescales of plagioclase crystal growth, using experimental growth rates[17,18]. The slope of the CSD is of -7.69 (Supplementary Table 4).

	Experiment
Felsic end-member	Dacite
Mafic end-member	Basalt
Duration of the mixing protocol (hours)	10.5
Temperature (°C)	1200
Pressure (atm)	1.00
H_2O (wt%)	0.00
Volume of felsic end-member (vol%)	80
Volume of mafic end-member (vol%)	20
Crystal content in the felsic end-member (area %)	0.00
Crystal content in the mafic end-member (area %)	0.00

Supplementary Table 6: Experimental conditions adopted during the magma mixing experiment.

References

1. Churikova, T. G. *et al.* Major and trace element zoning in plagioclase from Kizimen Volcano (Kamchatka): Insights into magma-chamber processes. *J. Volcanol. Seismol.* **7**, 112–130 (2013).
2. Churikova, T. G., Wörner, G., Eichelberger, J. & Ivanov, B. Minor- and trace element zoning in plagioclase from Kizimen Volcano, Kamchatka: Insights on the magma chamber processes. in *Volcanism and Subduction: The Kamchatka Region* 303–323 (2007). doi:10.1029/172GM22.
3. Giordano, D., Russell, J. K. & Dingwell, D. B. Viscosity of magmatic liquids: A model. *Earth Planet. Sci. Lett.* **271**, 123–134 (2008).
4. Gualda, G. A. R., Ghiorso, M. S., Lemons, R. V. & Carley, T. L. Rhyolite-MELTS: a Modified Calibration of MELTS Optimized for Silica-rich, Fluid-bearing Magmatic Systems. *J. Petrol.* **53**, 875–890 (2012).
5. Morgavi, D., Petrelli, M., Vetere, F. P., González-García, D. & Perugini, D. High-temperature apparatus for chaotic mixing of natural silicate melts. *Rev. Sci. Instrum.* **86**, 105108 (2015).
6. Swanson, P. D. & Ottino, J. M. A comparative computational and experimental study of chaotic mixing of viscous fluids. *J. Fluid Mech.* **213**, 227 (1990).
7. Galaktionov, O. S., Anderson, P. D., Peters, G. W. M. & Meijer, H. E. H. Mapping approach for 3D laminar mixing simulations: application to industrial flows. *Int. J. Numer. Methods Fluids* **40**, 345–351 (2002).
8. Rossi, S. *et al.* Role of magma mixing in the pre-eruptive dynamics of the Aeolian Islands volcanoes (Southern Tyrrhenian Sea, Italy). *Lithos* **324**–**325**, 165–179 (2019).
9. Rossi, S. *et al.* Exponential decay of concentration variance during magma mixing: Robustness of a volcanic chronometer and implications for the homogenization of chemical

heterogeneities in magmatic systems. *Lithos* **286**–**287**, 396–407 (2017).
10. Morgan, D. J. & Jerram, D. A. On estimating crystal shape for crystal size distribution analysis. *J. Volcanol. Geotherm. Res.* **154**, 1–7 (2006).
11. Bernard, O. & Bouvet de Maisonneuve, C. Controls on eruption style at Rabaul, Papua New Guinea – Insights from microlites, porosity and permeability measurements. *J. Volcanol. Geotherm. Res.* **406**, 107068 (2020).
12. Blundy, J. & Cashman, K. Petrologic Reconstruction of Magmatic System Variables and Processes. *Rev. Mineral. Geochemistry* **69**, 179–239 (2008).
13. Higgins, M. D. Measurement of crystal size distributions. *Am. Mineral.* **85**, 1105–1116 (2000).
14. Higgins, M. D. Closure in crystal size distributions (CSD), verification of CSD calculations, and the significance of CSD fans. *Am. Mineral.* **87**, 171–175 (2002).
15. Arzilli, F. *et al.* The unexpected explosive sub-Plinian eruption of Calbuco volcano (22–23 April 2015; southern Chile): Triggering mechanism implications. *J. Volcanol. Geotherm. Res.* **378**, 35–50 (2019).
16. Marshall, D. Ternplot: An excel spreadsheet for ternary diagrams. *Comput. Geosci.* **22**, 697–699 (1996).
17. Arzilli, F. *et al.* Plagioclase nucleation and growth kinetics in a hydrous basaltic melt by decompression experiments. *Contrib. to Mineral. Petrol.* **170**, 55 (2015).
18. Arzilli, F. *et al.* Magma fragmentation in highly explosive basaltic eruptions induced by rapid crystallization. *Nat. Geosci.* **12**, 1023–1028 (2019).